Formation of rolls from liquid crystal elastomer bistrips

Journal:	*Soft Matter*
Manuscript ID	SM-ART-12-2021-001830.R2
Article Type:	Paper
Date Submitted by the Author:	11-May-2022
Complete List of Authors:	Chen, Yuzhen; University of California Los Angeles, Mechanical and Aerospace Engineering Kuenstler, Alexa; University of Colorado Boulder, Chemical and Biological Engineering Hayward, Ryan; University of Colorado Boulder, Chemical and Biological Engineering Jin, Lihua; University of California Los Angeles, Mechanical and Aerospace Engineering

Title: Formation of rolls from liquid crystal elastomer bistrips

Yuzhen Chen[a], Alexa S. Kuenstler[b], Ryan C. Hayward[b]*, Lihua Jin[a]*

[a]Department of Mechanical and Aerospace Engineering, University of California, Los Angeles, CA 90095, USA

[b]Department of Chemical and Biological Engineering, University of Colorado Boulder, CO 80309, USA

*Corresponding Authors

Email: Ryan.Hayward@colorado.edu, lihuajin@seas.ucla.edu

Abstract

Formation of desired three-dimensional (3D) shapes from flat thin sheets with programmed non-uniform deformation profiles is an effective strategy to create functional 3D structures. Liquid crystal elastomers (LCEs) are of particular use in programmable shape morphing due to their ability to undergo large, reversible, and anisotropic deformation in response to a stimulus. Here we consider a rectangular monodomain LCE thin sheet divided into one high- and one low-temperature strip, which we dub a 'bistrip'. Upon activation, a discontinuously patterned, anisotropic in-plane stretch profile is generated, and induces buckling of the bistrip into a rolled shape with a transitional bottle neck. Based on the non-Euclidean plate theory, we derive an analytical model to quantitatively capture the formation of the rolled shapes from a flat bistrip with finite thickness by minimizing the total elastic energy involving both stretching and bending energies. Using this analytical model, we identify the critical thickness at which the transition from the unbuckled to buckled configuration occurs. We further study the influence of the anisotropy of the stretch profile on the rolled shapes by first converting prescribed metric tensors with different anisotropy to a unified metric tensor embedded in a bistrip of modified geometry, and then investigating the effect of each parameter in this unified metric tensor on the rolled shapes. Our analysis sheds light on designing shape morphing of LCE thin sheets, and provides quantitative predictions on the 3D shapes that programmed LCE sheets can form upon activation for various applications.

Keywords

liquid crystal elastomers, shape morphing, non-Euclidean plate, buckling, finite thickness, anisotropy

1. Introduction

Shape morphing from an initially flat sheet to a desired three-dimensional (3D) shape triggered by a stimulus is an effective approach for fabricating complex 3D structures with advanced functionalities. By patterning spatially varied stimuli-induced strain, shape morphing has been achieved in various responsive materials, such as hydrogels[1–4], liquid crystal elastomers (LCEs)[5–10], and shape memory polymers[11,12]. These two-dimensional (2D)-to-3D shape transitions have been used in a wide range of applications, including biomedical devices[13,14], soft actuators and sensors[15,16], and mechanical metamaterials[17,18].

To transition a flat sheet to a desired 3D shape, it is necessary to induce spatially non-uniform stresses inside the material upon activation[19,20]. A through-thickness stress variation can generate a bending moment and thus out-of-plane deformation. An in-plane stress variation, on the other hand, can drive out-of-plane buckling of a flat sheet into a 3D shape. Although both types of stress variations can trigger shape transition of a flat sheet to 3D shape, the buckling-induced shape transition relying on in-plane stress variations has the following three advantages: (1) it broadens the accessible 3D shapes incorporating both Gaussian and mean curvatures; (2) it requires patterning of only a single material layer, which can be easily achieved using numerous 2D patterning techniques such as lithography[2,10,21–23], direct ink writing[3,24,25], and laser cutting[26]; (3) buckling-induced shapes are much more robust to external loads than those induced by pure bending, since the energy to deform the former scales with the film thickness $\sim h$, while the energy to deform the latter scales as $\sim h^3$ [7,27,28].

Though many systems have been explored for their use in shape morphing, LCEs are particularly useful due to the coupling of orientational order of constituent mesogens with polymer conformation[5,7,16]. Upon activation by heating, the orientational order of mesogens reduces, yielding large and anisotropic deformation. Recently, we demonstrated a method[10] to prescribe various in-plane stretch profiles to a flat monodomain LCE sheet by spatially patterning the concentration of plasmonic gold nanoparticles which produce heat upon illumination. Under uniform illumination, a non-uniform distribution of gold nanoparticles causes a gradient in photothermal heat generation, and therefore non-uniform in-plane stretch, yielding out-of-plane buckling of the flat sheet. Compared to spatially programming director orientation[7,8,24,25,29–32], this method can be widely generalized to most LCE systems with a simple fabrication process. The shape morphing of flat LCE sheets with prescribed in-plane stretch profiles can be captured by the non-Euclidean plate theory[33,34], which, like the Föppl-von Kármán (FvK) plate theory[35], takes into account both bending and stretching energies. In this theory, strains are measured with respect to a reference metric tensor, which is defined by the prescribed in-plane stretch profile and is not necessarily immersible in a 3D Euclidean space. In our previous study[10], we have linked a prescribed in-plane stretch profile to the 3D shape for a LCE sheet with an infinitesimal thickness by minimizing the bending energy among all the isometric immersions, in which the actual metric tensors fully obey the prescribed metric tensors, leading to zero stretching energy. As the thickness increases, the actual metric tensor deviates from the prescribed metric tensor as a result of the interplay between the bending and stretching energies. In this paper, we will address the thickness effect on the shape morphing of LCE sheets.

To study this problem, we choose the simple bistrip geometry, where a rectangular monodomain LCE sheet is divided into two strips, i.e. the high- and low-temperature strips (Fig. 1A). The high-temperature strip contains gold nanoparticles (dark strips in Fig. 1B), and generates more photothermal heat upon illumination than the low-temperature strip that contains no gold nanoparticles (transparent strips in Fig. 1B), leading to a nearly step distribution in temperature (Fig. 1A) and thus a discretely patterned in-plane stretch profile. As a LCE shrinks along the director and elongates in the perpendicular direction upon heating, the induced stretch profile in a bistrip LCE highly depends on its initial director. We find in both experiments (Fig. 1B) and finite element (FE) simulations (Fig. 1C) that upon illumination, a bistrip, with the initial director $\mathbf{n}$ either parallel (left) or perpendicular (right) to the interface between the two strips, can roll into a nearly axisymmetric shape, which consists of two nearly cylindrical regions smoothly connected via a transitional bottle neck. However, the rolled shape is strongly affected by the anisotropy of the prescribed stretch profile. There are extensive studies on the rolled shape formation in isotropically deformed gel bistrips[21,36,37], but not on anisotropically deformed LCE bistrips, to the best of our knowledge.

In this paper, we establish an analytical model based on the non-Euclidean plate theory to capture the rolled shapes from LCE bistrips with finite thicknesses, and identify the critical thickness at which the transition from an unbuckled to buckled configuration occurs. To investigate the influence of the stretch anisotropy on the rolled shapes, we convert the prescribed metric tensors in LCE bistrips with initial director either parallel or perpendicular to the interface into a unified metric tensor embedded in a bistrip with modified geometry. Using this analytical model, we study the effect of each parameter in the unified metric tensor on the rolled shapes from bistrips. The quantitative agreement between the analytical model and FE simulations validates our analysis.

2. Modeling shape morphing of LCE bistrips

We model a bistrip of length L, width w, and thickness h (Fig. 1A) using the reduced 2D non-Euclidean plate theory[33,34,36], in which the bistrip is represented by its mid-surface, and the prescribed metric tensor $\bar{\boldsymbol{a}}$ of this mid-surface may not be immersible in a 3D Euclidean space. $\bar{\boldsymbol{a}}$ of the bistrip is determined by a prescribed in-plane stretch profile,

$$\bar{\boldsymbol{a}} = \begin{bmatrix} \lambda_u^2 & 0 \\ 0 & \lambda_v^2 \end{bmatrix}, \tag{1}$$

where u and v are the two surface coordinates of the mid-surface (Fig. 2A), and λ_u and λ_v are the discretely patterned in-plane stretches in the u and v directions, respectively. The two stretches λ_u and λ_v are assumed to depend solely on v, which can be described by the following sigmoid functions:

$$\lambda_u = \bar{\lambda}_u - \frac{\Delta_u}{1 + e^{-\frac{v/w - \rho}{\delta/w}}}, \lambda_v = \bar{\lambda}_v - \frac{\Delta_v}{1 + e^{-\frac{v/w - \rho}{\delta/w}}}, \tag{2}$$

where $\bar{\lambda}_u$ ($\bar{\lambda}_v$) represents the stretch of the low-temperature strip in the u (v) direction, Δ_u (Δ_v) represents the stretch difference between the high- and low-temperature strips in the u (v) direction, ρ represents the width of the low-temperature strip normalized by the total width w, δ denotes the smoothness of the step change in the stretch, and $10\delta/w$ is defined as the normalized width of the transition region through which the stretch reduces by $0.99\Delta_u(\Delta_v)$ in the u (v) direction. A positive Δ_u (Δ_v) indicates $\lambda_u|_{v<\rho w} > \lambda_u|_{v>\rho w}$ ($\lambda_v|_{v<\rho w} > \lambda_v|_{v>\rho w}$). The anisotropic stretch profiles highly depend on the initial director **n** of LCE bistrips. We find that in our experiments when $\mathbf{n} \parallel u$, $\bar{\lambda}_u = 0.92$ and $\Delta_u = 0.15$[10] (Fig. 1A left; Appendix). The stretch in the v direction can be determined by incompressibility $\lambda_v = 1/\sqrt{\lambda_u}$, yielding $\bar{\lambda}_v = 1/\sqrt{\bar{\lambda}_u} = 1.04$ and $\Delta_v = 1/\sqrt{\bar{\lambda}_u} - 1/\sqrt{\bar{\lambda}_u - \Delta_u} = -0.097$. When $\mathbf{n} \parallel v$, $\bar{\lambda}_v = 0.92$ and $\Delta_v = 0.15$ (Fig. 1A right). Correspondingly, $\bar{\lambda}_u = 1.04$ and $\Delta_u = -0.097$ due to incompressibility. The Gaussian curvature $\bar{K}$ corresponding to the prescribed metric tensor $\bar{\boldsymbol{a}}$ is[38]

$$-\bar{E}\bar{K} = -\bar{\Gamma}_{11}^{2\,\prime} + \bar{\Gamma}_{12}^{1}\bar{\Gamma}_{11}^{2} + \bar{\Gamma}_{12}^{2}\bar{\Gamma}_{12}^{2} - \bar{\Gamma}_{11}^{2}\bar{\Gamma}_{22}^{2} - \bar{\Gamma}_{11}^{1}\bar{\Gamma}_{12}^{2}, \tag{3}$$

where $\bar{E} = \lambda_u^2$, $()'$ denotes the derivative with respect to v, and $\bar{\Gamma}_{\beta\gamma}^{\alpha}$ $(\alpha, \beta, \gamma = 1, 2)$ are the Christoffel symbols of $\bar{\boldsymbol{a}}$ and equal

$$\bar{\Gamma}_{11}^{1} = 0, \bar{\Gamma}_{12}^{1} = \bar{\Gamma}_{21}^{1} = \frac{\lambda_u'}{\lambda_u}, \bar{\Gamma}_{22}^{1} = 0, \bar{\Gamma}_{11}^{2} = -\frac{\lambda_u\lambda_u'}{\lambda_v^2}, \bar{\Gamma}_{12}^{2} = \bar{\Gamma}_{21}^{2} = 0, \bar{\Gamma}_{22}^{2} = \frac{\lambda_v'}{\lambda_v}. \tag{4}$$

Substituting Eq. (4) into Eq. (3) yields

$$\bar{K} = \frac{\lambda_u'\lambda_v' - \lambda_u''\lambda_v}{\lambda_u\lambda_v^3}. \tag{5}$$

Based on the non-Euclidean plate theory[33,34,36], the elastic energy of the bistrip can be expressed as

$$E_{\text{total}} = E_{\text{stretch}} + E_{\text{bend}}, \tag{6}$$

where E_{stretch} is the stretching energy

$$E_{\text{stretch}} = \frac{\mu h}{4}\int_0^L\int_0^w (\bar{a}^{\alpha\beta}\bar{a}^{\gamma\eta} + \bar{a}^{\alpha\gamma}\bar{a}^{\beta\eta})(a-\bar{a})_{\alpha\beta}(a-\bar{a})_{\gamma\eta}\sqrt{|\bar{\boldsymbol{a}}|}\,dvdu, \tag{7}$$

and E_{bend} is the bending energy

$$E_{\text{bend}} = \frac{\mu h^3}{12}\int_0^L\int_0^w (\bar{a}^{\alpha\beta}\bar{a}^{\gamma\eta} + \bar{a}^{\alpha\gamma}\bar{a}^{\beta\eta})b_{\alpha\beta}b_{\gamma\eta}\sqrt{|\bar{\boldsymbol{a}}|}\,dvdu. \tag{8}$$

In Eqs. (7) and (8), $\boldsymbol{a}$ is the actual metric tensor and $\boldsymbol{b}$ is the actual curvature tensor of the mid-surface. The actual Gaussian curvature K can be expressed in terms of the components of $\boldsymbol{a}$ and their derivatives[38]. The stretching energy in Eq. (7) is associated with changes of distances in the mid-surface from its prescribed metric tensor $\bar{\boldsymbol{a}}$, and the bending energy in Eq. (8) is associated with changes of curvatures from the flat configuration. Note that $E_{\text{stretch}} \sim h$ and $E_{\text{bend}} \sim h^3$. When the bistrip is extremely thin ($h \to 0$), it prefers obeying its prescribed metric tensor $\bar{\boldsymbol{a}}$ such that $E_{\text{stretch}} \to 0$, and the total energy goes with E_{bend}. We call this condition as the thin limit or isometric immersion. When the bistrip is extremely thick ($h\sqrt{K} \gg 1$), it remains flat with only in-plane stretching such that $E_{\text{bend}} = 0$, and the total energy goes with E_{stretch}. We call this condition as the thick limit. Within these two limits, the 3D shape of the bistrip is determined by the interplay between E_{stretch} and E_{bend}.

Next, we try to minimize the elastic energy E_{total} in Eq. (6) with the prescribed metric tensor $\bar{\boldsymbol{a}}$ in Eq. (1). Given that the bistrips consistently roll into axisymmetric shapes in the experiments (Fig. 1), we seek solutions under the assumption of surface of revolution. Therefore, the actual metric tensor $\boldsymbol{a}$ and curvature tensor $\boldsymbol{b}$ are assumed to depend solely on the axial coordinate v. With appropriate parameterization, $\boldsymbol{a}$ and $\boldsymbol{b}$ can be diagonal, i.e.

$$\boldsymbol{a} = \begin{bmatrix} E(v) & 0 \\ 0 & G(v) \end{bmatrix}, \boldsymbol{b} = \begin{bmatrix} e(v) & 0 \\ 0 & g(v) \end{bmatrix}. \tag{9}$$

Based on the Gauss formula and Mainardi-Codazzi equations[36,38], the terms $e(v)$ and $g(v)$ in $\boldsymbol{b}$ can be expressed in terms of $E(v)$ and $G(v)$:

$$e^2 = cE - \frac{E'^2}{4G}, \tag{10}$$

$$g^2 = \frac{\left(E'^2G + EE'G' - 2EE''G\right)^2}{4E^2G\left(4cEG - E'^2\right)}, \tag{11}$$

where c is an integration constant. To determine the shape of the mid-surface, we need to find $E(v)$, $G(v)$, and c such that E_{total} in Eq. (6) is minimized. This minimization can be performed by either numerical optimization or a variational approach (Appendix). Since the two methods are equivalent, here we only show the numerical optimization.

The process of the numerical optimization is as follows. First, we uniformly discretized the domain of v into m points with an increment ${}^{w}/_{(m-1)}$. Then $E(v)$, $G(v)$, $e(v)$, and $g(v)$ were also discretized. We used E_i, G_i, e_i, and g_i $(i = 1, ..., m)$ to represent their values at point v_i $(0 \leq v_i \leq w)$, respectively. Second, we expressed e_i, and g_i in terms of E_i, G_i, and c using Eqs (10) and (11), in which the derivative terms are approximated by the finite difference. Finally, we used unconstrained nonlinear programming solver (fminunc) in Matlab to solve the following minimization problem

$$\min_{E_i,\, G_i,\, c} E_{\text{total}}, (i = 1, ..., m), \tag{12}$$

where E_i, G_i, and c are to be determined. This minimization problem was solved iteratively for various thicknesses. We started from the case with an extremely small thickness, i.e. ${}^{h}/_{w} = 10^{-6}$, and used the solution of isometric immersion as the initial try, in which $\boldsymbol{a} = \bar{\boldsymbol{a}}$ and $\boldsymbol{b}$ is determined by minimizing E_{bend}. Then we gradually increased the thickness and used the solution of the previous step as an initial try of the current step. This iteration stopped as the bending energy becomes negligible $\left({}^{E_{\text{bend}}}/_{E_{\text{total}}} \leq 0.001\right)$.

To demonstrate the process of minimizing E_{total}, we take a bistrip with $L/w = 2.0$ and the initial director $\mathbf{n}$ parallel to the interface between high- and low-temperature strips as an example. In Figs. 2B and C, we can see how E_{total}/h (black dots), E_{bend}/h (blue dots), and E_{stretch}/h (red dots) evolve with h/w. When h/w is very small, the majority of E_{total} is E_{bend}. As h/w increases, E_{bend} first increases and then reduces to nearly zero, whereas E_{stretch} increases monotonically and becomes dominant. We define the thickness at which $E_{\text{bend}}/E_{\text{total}}$ decreases to below 0.001 as the critical thickness h_{cr}. When h/w is below h_{cr}/w, the bistrip is considered in a buckled configuration. When h/w is above h_{cr}/w, E_{stretch} approaches E_{total}, while E_{bend} goes to zero, indicating an unbuckled configuration.

Besides, we found the following scaling relations when h/w is very small (Fig. 2C),

$$E_{\text{stretch}}/h \sim h^4,\ E_{\text{bend}}/h \sim h^2. \tag{13}$$

As shown in Eq. (7), E_{stretch}/h is proportional to the quadratic of the differences between the components of $\boldsymbol{a}$ and $\bar{\boldsymbol{a}}$. We plot the distributions of the metric differences $\boldsymbol{a} - \bar{\boldsymbol{a}}$ in the u (Fig. 2D upper) and v (Fig. 2D lower) directions for bistrips with very small h/w, and find that $\boldsymbol{a} = \bar{\boldsymbol{a}}$ except a transition region, and the length of the transition region is unaffected by h/w. The maximum magnitudes of the metric differences in the u and v directions are found to scale with $(h/w)^2$ when h/w is very small (Fig. 2E). Therefore, the quadratic increase of the metric differences with h/w in a transition region results in the fourth power scaling relation between E_{stretch}/h and h. E_{bend}/h, on the other hand, not only scales quadratically with the curvature tensor $\boldsymbol{b}$, but also scales with h^2, as shown in Eq. (8). By plotting the distributions of $\boldsymbol{b}$ in the u (Fig. 2F upper) and v (Fig. 2F lower) directions for bistrips with very small h/w, we find that $\boldsymbol{b}$ is independent of h/w. Thus, E_{bend}/h and h show a quadratic power-law relation.

Once $\boldsymbol{a}$ and $\boldsymbol{b}$ are obtained by minimizing E_{total}, the shape of the bistrip can be uniquely determined (Appendix). In Fig. 3, we plot the 3D shapes obtained from our analytical model (Fig. 3A-C, Appendix), and compare them with the ones obtained from the FE simulations (Fig. 3D-F, Appendix) for

h/w = 0.005 (A and D), 0.015 (B and E), and 0.025 (C and F). Both the theory and the FE simulations show that the bistrips roll around an axis perpendicular to the interface between the high- and low-temperature strips. The rolled shape is composed of two nearly cylindrical regions connected by a transitional bottle neck in which the Gaussian curvature alters from positive to negative. We define the width of this transitional bottle neck region w_{trans} as the distance between the maximum and the minimum Gaussian curvatures (Fig. 3A). Away from the transitional bottle neck region, $\boldsymbol{a}$ obeys $\bar{\boldsymbol{a}}$, and the Gaussian curvature is zero due to the homogeneous prescribed stretch. Thus, the stretching energy is mainly concentrated within the bottle neck and favors a smaller w_{trans}, whereas the bending energy is distributed throughout the entire sheet and favors a smaller curvature. Both w_{trans} and the curvature of the rolled shape are determined by the competition between the stretching within the bottle neck and the bending across the entire sheet. As the thickness of the bistrip increases, $\boldsymbol{a}$ deviates more from $\bar{\boldsymbol{a}}$. Accordingly, the portion of the stretching energy increases and the portion of bending energy decreases, yielding an increase in w_{trans} and decrease in curvature (Fig. 3A-F). In Fig. 3G and H, we plot the profiles of the cross-section along (G) and perpendicular (H) to the interface between the high- and low-temperature strips, and show that the theory (circular dots) and the FE simulations (solid lines) are in quantitative agreement, which validates our theory. The slight deviation at the edges results from the boundary effect that undermines the axisymmetric assumption.

To further validate our analytical model, we study the rolled shape formation from bistrips with different normalized widths of the low-temperature strip ρ ranging from 0.2 to 0.8 (Fig. 4A). All the bistrips have $L/w = 1.0$, $h/w = 0.005$, and initial director parallel to the interface between the high- and low-temperature strips. Fig. 4B-D show the deformed shapes of the bistrips obtained from experiments (Fig. 4B), FE simulations (Fig. 4C), and theory (Fig. 4D), from which we can see that the bistrips roll around an axis perpendicular to the interface and form a transitional bottle neck at the interface, regardless of ρ. The bottle neck moves along the rolling axis while maintains its width w_{trans} as ρ increases. The FE simulations can quantitatively capture the rolled shapes observed in the experiments.

The theory can provide good predictions on the rolled shapes close to the bottle neck. Near the edges of the bistrips, the shapes predicted by the theory deviate from those obtained in the FE simulations, since the axisymmetric assumption in the theory no longer holds there.

3. Influence of stretch anisotropy on the formation of rolls from LCE bistrips

We learn from Fig. 1 that a bistrip with the initial director either parallel or perpendicular to the interface between the high- and low-temperature strips can roll into approximately axisymmetric shapes upon activation. However, the rolled shapes for the parallel and perpendicular cases are different, indicating that the shape morphing depends on the anisotropy of the prescribed in-plane stretch. In this section, we study the influence of the stretch anisotropy on the rolled shapes. We first show that a bistrip with a prescribed metric tensor of different anisotropy, corresponding to initial director either parallel or perpendicular to the interface, can be converted to a bistrip of modified geometry with a unified metric tensor. Then we investigate how each parameter in this unified metric tensor influences the formation of rolled shapes from LCE bistrips.

Suppose we have a bistrip of length L, width w, thickness h, and the metric tensor $\bar{\boldsymbol{a}}$ in Eq. (1) is applied onto this bistrip (Fig. 5A). Given that $\bar{\boldsymbol{a}}$ is diagonal, it can be divided into the parts without stretch mismatch $\bar{\boldsymbol{a}}_1$, $\bar{\boldsymbol{a}}_2$, and the part with stretch mismatch and thus generating in-plane stresses, $\bar{\boldsymbol{a}}^*$ (Appendix), where

$$\bar{\boldsymbol{a}}_1 = \begin{bmatrix} 1 & 0 \\ 0 & \lambda_v^2 \end{bmatrix}, \bar{\boldsymbol{a}}_2 = \begin{bmatrix} (\bar{\lambda}_u)^2 & 0 \\ 0 & 1 \end{bmatrix}, \bar{\boldsymbol{a}}^* = \begin{bmatrix} (\lambda_u^*)^2 & 0 \\ 0 & 1 \end{bmatrix}, \tag{14}$$

corresponding to a stress-free deformation in the v direction, and a homogeneous and an inhomogeneous deformation in the u direction, respectively, and

$$\lambda_u^* = \lambda_u / \bar{\lambda}_u. \tag{15}$$

Please note that this decomposition of $\bar{\boldsymbol{a}}$ into $\bar{\boldsymbol{a}}_1$, $\bar{\boldsymbol{a}}_2$, and $\bar{\boldsymbol{a}}^*$ holds only if $\bar{\boldsymbol{a}}$ is diagonal, as shown in Eq. (1). Since shape morphing of LCE bistrips is elastic and conservative, the obtained shape should be independent of loading paths. Therefore, applying $\bar{\boldsymbol{a}}_1$, $\bar{\boldsymbol{a}}_2$, and $\bar{\boldsymbol{a}}^*$ one by one (Path 2 in Fig. 5A) should result in the same 3D shape as applying $\bar{\boldsymbol{a}}$ once (Path 1 in Fig. 5A). After $\bar{\boldsymbol{a}}_1$ is applied, the bistrip is stretched along the v direction by λ_v. As a consequence, the current width of the bistrip w^* becomes

$$w^* = \int_0^w \lambda_v(v)\mathrm{d}v, \tag{16}$$

and the current surface coordinate v^* can be expressed as

$$v^* = \int_0^v \lambda_v(\tau)\mathrm{d}\tau. \tag{17}$$

After $\bar{\boldsymbol{a}}_2$ is applied, the bistrip is stretched homogeneously along the u direction by $\bar{\lambda}_u$, yielding a new length $L^* = \bar{\lambda}_u L$ and a new surface coordinate $u^* = \bar{\lambda}_u u$. By far, the bistrip remains unbuckled, since no variation in the in-plane stress is generated. We further apply the metric tensor $\bar{\boldsymbol{a}}^*$ onto the bistrip with the new width w^* and length L^*. Note that $\bar{\boldsymbol{a}}^*$ only involves stretches λ_u^* in the u^* direction, which can be expressed with respect to v^* in the following unified form

$$\lambda_u^*(v^*) = 1 - \frac{\Delta_u^*}{1 + e^{-\frac{v^*/w^* - \rho^*}{\delta^*/w^*}}}, \tag{18}$$

where $\Delta_u^* = \Delta_u/\bar{\lambda}_u$, and ρ^* and δ^* can be obtained by finding the least-square fitting of Eq. (18) to a set of pairs (v^*, λ_u^*) given by combining Eqs. (15) and (17). By minimizing the total elastic energy, the rolled shape for the bistrip with $\bar{\boldsymbol{a}}^*$ and modified geometry can be determined.

To confirm that the rolled shapes following Path 1 and 2 (Fig. 5A) are identical, we consider a bistrip of thickness $h = 0.005w$ and length $L = 2w$, with an equal width of the high- and low-temperature strips and the initial director perpendicular to the interface between the two strips. Upon activation, the bistrip undergoes shrinkage in the v direction by λ_v, which can be quantified by Eq. (2) with $\bar{\lambda}_v = 0.92$, $\Delta_v = 0.15$, $\delta/w = 0.02$, and $\rho = 0.5$. Due to the incompressibility, the bistrip undergoes expansion in the u direction by $\lambda_u = 1/\sqrt{\lambda_v}$, yielding $\bar{\lambda}_u = 1.04$ and $\Delta_u = -0.097$. Given the in-plane stretch profiles, the prescribed metric tensor $\bar{\boldsymbol{a}}$ is determined, and the rolled shape can be then obtained using the analytical model (Path 1 in Fig. 5A). Following Path 2, the bistrip is first shrunk in the v direction by λ_v due to $\bar{\boldsymbol{a}}_1$, and then expanded in the u direction by $\bar{\lambda}_u$ due to $\bar{\boldsymbol{a}}_2$, resulting in a flat stress-free bistrip of a modified width $w^* = 0.845w$ and length $L^* = 2.085w$. Finally, $\bar{\boldsymbol{a}}^*$ involving stretch λ_u^* with $\Delta_u^* = -0.093$, $\rho^* = 0.544$ and $\delta^*/w = 0.0168$ is applied to the new bistrip, yielding a rolled shape that can be captured by the analytical model. In Fig. 5, we plot the 3D shapes predicted by the analytical model following Path 1 and 2 and the FE simulation, and compare their profiles of the cross-section along (B) and perpendicular to (C) the interface between the two strips. The rolled shapes from Path 1 and 2 match perfectly, indicating that the shape morphing following Path 1 and 2 is equivalent. The quantitative agreement between the theoretical predictions (circular dots) and the FE simulation results (solid lines) validates our theory (Fig. 5B and 5C).

Having converted a prescribed metric tensor in LCE bistrips with initial director either parallel or perpendicular to the interface into a unified metric tensor, we will next investigate the influence of each parameter in this unified metric tensor on the rolled shape formation from bistrips with a finite thickness. Note that bistrips with an infinitely small thickness ($h \rightarrow 0$) adopt the isometric immersion of $\bar{\boldsymbol{a}}^*$ that minimizes the bending energy. Using Eq. (5), we can obtain the Gaussian curvature,

$$K^* = -\frac{\lambda_u^{*''}}{\lambda_u^*}. \tag{19}$$

Then the width of the transitional bottle neck region w_{trans}^* can be obtained by

$$\frac{w_{\text{trans}}^*}{w^*} = \left.\frac{v^*}{w^*}\right|_{K_{\text{min}}^*} - \left.\frac{v^*}{w^*}\right|_{K_{\text{max}}^*} \approx 2.634\frac{\delta^*}{w^*}, \tag{20}$$

where $\left.\frac{v^*}{w^*}\right|_{K_{\text{max}}^*}$ and $\left.\frac{v^*}{w^*}\right|_{K_{\text{min}}^*}$ are the normalized v^* that maximizes and minimizes K^*, respectively, and can be computed by solving $K^{*\prime} = 0$. From Eq. (20) we can see that w_{trans}^* depends only on δ^*/w^* for bistrips with an infinitely small thickness. Next, we will show that as the thickness becomes finite, more parameters play roles in influencing w_{trans}^*. For convenience, we will remove all the "*" in Eq. (18).

We first investigate the effect of the stretch mismatch Δ_u between the high- and low-temperature strips on the rolled shapes, as shown in Fig. 6. We fix $\rho = 0.5$ and $\delta/w = 0.02$, while changing Δ_u from 0.002 to 0.1. As Δ_u increases, the critical thickness h_{cr}/w, which is defined as the thickness at which $E_{\mathrm{bend}}/E_{\mathrm{total}} = 0.001$, also increases (Fig. 6A), indicating that a higher stretch mismatch can trigger buckling of a thicker bistrip into a rolled shape. When $h = 0$ (black lines in Fig. 6B and 6C), the isometric immersion containing zero stretching energy is adopted. An increase in Δ_u leads to more bending energy and thus larger average mean curvature H_{avg} over the entire width (black line in Fig. 6B). The width of the transitional bottle neck w_{trans} is unaffected by Δ_u and equals $2.634\delta/w = 0.0527$ (Eq. (20)) (black line in Fig. 6C). As h increases, the actual metric deviates from the prescribed metric within the bottle neck, yielding an increase in the portion of stretching energy and a decrease in the portion of bending energy. Correspondingly, w_{trans} increases (Fig. 6C) and H_{avg} decreases (Fig. 6B) for an increasing h and a fixed Δ_u. Furthermore, a bistrip with finite h bends more (larger H_{avg}) for a larger Δ_u (Fig. 6B and 6D-G). Its transitional bottle neck region occupies almost the entire width ($w_{\mathrm{trans}} \rightarrow w$) when Δ_u is infinitely small, and quickly shrinks and becomes saturated as Δ_u increases (Fig. 6C-G).

We then study how the smoothness of the step change in the stretch profile δ influences the rolled shapes. In Fig. 7, we fix $\rho = 0.5$ and $\Delta_u = 0.05$, while changing δ/w from 0.01 to 0.06. As δ/w increases, i.e. the step change in the stretch profile becomes smoother, the critical thickness h_{cr}/w decreases (Fig. 7A). The bistrip adopting an isometric immersion ($h = 0$) bends less (smaller H_{avg}) for a smoother stretch profile (larger δ/w) (black line in Fig. 7B). Its w_{trans}/w linearly increases with δ/w at a rate of 2.634 (Eq. (20)) (black line in Fig. 7C). For bistrips with non-zero h, their H_{avg} decreases (Fig. 7B and 7D-G) and w_{trans} increase (Fig. 7C-G), with an increasing δ. The H_{avg}-δ and w_{trans}-δ relations shift downward (Fig. 7B) and upward (Fig. 7C), respectively, as h increases due to the same reason as discussed in Fig. 6B and C.

Furthermore, we study how the normalized width of the low-temperature strip ρ influences the rolled shapes (Fig. 8). We fix $\delta/w = 0.02$ and $\Delta_u = 0.05$, while changing ρ from 0.2 to 0.8. As ρ increases, the interface between the high- and low-temperature strips moves along the width direction. Correspondingly, the critical thickness h_{cr}/w changes non-monotonically: it first increases and then decreases as the interface moves from the edge to the center of the bistrips (Fig. 8A). This non-monotonic change is because the regions near the free boundaries have less constraints on bending, and thus even thick bistrips prefer bending to stretching if the interface is close to the free boundary. However, an interface too close to the free boundary leads to an incomplete bottle neck, yielding higher constraints on bending and thus smaller h_{cr}. Unlike the effect of Δ_u and δ/w, ρ has a very limited effect on H_{avg} (Fig. 8B, 8D-G) and w_{trans} (Fig. 8C-G). Similar to Fig. 6 and 7, as h increases, H_{avg} decreases (Fig. 8B) and w_{trans} increases (Fig. 8C).

We summarize the influence of Δ_u, δ, and ρ defined in Eq. (18), as well as thickness h on the shape morphing of rolled shapes as follows. A larger stretch mismatch Δ_u can trigger the formation of rolled shapes from thicker bistrips and cause a larger curvature H_{avg} for bistrips with $h < h_{\mathrm{cr}}$, but has little influence on the width of the transitional bottle neck w_{trans} when Δ_u is not small. A smoother step change in the stretch profile, i.e. larger δ, reduces the critical threshold h_{cr} and H_{avg}, but enlarges w_{trans}. ρ only changes the position of the bottle neck but not w_{trans} and H_{avg}. As the bottle neck approach the free boundaries, h_{cr} increases. For a given stretch profile (Δ_u, δ, and ρ are fixed), a thicker bistrip tends to bend less (smaller H_{avg}) and has a wider bottle neck (larger w_{trans}).

4. Conclusion

In this paper, we have studied the rolled shape formation from LCE bistrips subjected to discretely patterned in-plane stretch profiles. We establish an analytical model based on the non-Euclidean plate theory, which can predict the shape morphing of LCE bistrips with finite thicknesses from flat to rolled shapes by minimizing the total elastic energy. Our analytical model, FE simulations, and experiments are in good agreement, which verifies our theory. We find that when the thickness h is very small, the bending energy E_{bend} is dominant and E_{bend}/h scales with h^2, whereas the stretching energy E_{stretch}/h scales with h^4. As h increases and eventually reaches the critical thickness h_{cr}, E_{stretch}/h becomes dominant and E_{bend}/h reduces to zero. To investigate the influence of the anisotropy of the stretch on the rolled shapes, we convert the prescribed metric tensors in LCE bistrips with initial director either parallel or perpendicular to the interface into a unified metric tensor embedded to a bistrip with modified geometry. We then study the effect of each parameter in this unified metric tensor and the thickness on the critical thickness, average curvature, and the bottle neck width of the rolled shapes. As a result, as the stretch mismatch Δ_u increases or the step of the stretch profile δ decreases, the critical thickness h_{cr} increases, the average mean curvature H_{avg} increases, and the width of the transitional bottle neck w_{trans} decreases until a saturated value. The normalized width of the low-temperature strip ρ only changes the position of the bottle neck and the critical thickness h_{cr}, but not w_{trans} and H_{avg}. Our analysis provides an analytical tool for designing shape morphing using LCE thin sheets, and can be extended to shape morphing of other isotropic or anisotropic materials.

Appendix

1. LCE fabrication

Liquid crystal elastomer nanocomposites were prepared as previously reported[10]. The diacrylate mesogen RM82, *n*-dodecylamine, and 8-amino-1-octanol were mixed in a 1.1:0.5:0.5 molar ratio with 1 wt% Irgacure 651 in a vial and melted to form a mesogenic liquid. The molten mixture was subsequently infiltrated via capillary action into alignment cells consisting of two glass slides coated with Elvamide polyimide (DuPont), rubbed with a velvet cloth, and glues together with 50 μm glass spacer beads. Next, samples were held at 55 °C overnight to catalyze oligomerization of the oligomers and subsequently polymerized at room temperature under UV light (10 mW cm^{-2}). Following polymerization, LCE films were harvested from the cells using a razor blade.

2. Nanocomposite fabrication

A gold nanoparticle precursor solution was prepared from 200 µL of $HAuCl_4$ in acetone (0.12 M), 200 µL of oleylamine in toluene (0.44 M), and Irgacure (0.44 M). The solution was subsequently diluted with 800 µL toluene and vortexed vigorously, and LCE films cut to the desired dimensions were submersed in the solution. The films were allowed to absorb the gold-containing solution for several minutes. Following equilibrium swelling, films were removed from the solution, blotted gently with tissue paper to remove excess solution, placed on a glass slide, and sandwiched between a photomask. Photomasks were prepared in Adobe Illustrator and printed on transparency films (Apollo Laser Printer Transparency Film). Samples were patterned via exposure with 30 mW cm^{-2} 365 nm light (ThorLabs) for 10 s, immersed in acetone for 60 min to remove unreacted gold salt, and dried under gentle vacuum. Nanocomposite absorbance was controlled by modulating the light dose via grayscale photomasks that vary from 0% black (transparent) to 100% black (opaque). To specify the actuation behavior described in this work, LCE bistrips were created by using a photomask with a 0% black strip and a 100% black strip, yielding materials with a photothermal (i.e. high temperature) and non-photothermal (i.e. low temperature) strip, respectively.

3. Photoactuation experiments

To evaluate shape morphing of patterned LCE bistrips upon illumination, samples were held isothermally on a hot plate at 85 °C and illuminated with a 530 nm green LED (200 mW cm^{-2}). Depending on the transparency of the photomask, the stretch λ due to photothermal heating can be programmed from 0.77 (0% black) to 0.92 (100% black). Shape transformations were recorded using a camera (Nikon 5500) fitted with a macro lens.

4. Finite element simulations

The LCE sheets were modeled using the following neo-classical free energy density[39,40]

$$\psi = \frac{\mu}{2}\left[\mathrm{Tr}\left(\tilde{\boldsymbol{g}}^{-1}\mathbf{F}\tilde{\boldsymbol{g}}_0\mathbf{F}^{\mathrm{T}}\right) - 3\right] + \frac{K}{2}(J-1)^2 - \mu\ln J, \tag{A1}$$

where μ is the shear modulus, K is the bulk modulus, $\mathbf{F}$ is the deformation gradient and $J = \det(\mathbf{F})$, $\tilde{\boldsymbol{g}}$ is a temperature-dependent three-dimensional normalized step-length tensor that describes the anisotropy of LCEs with respect to the isotropic phase in the current configuration[40], and $\tilde{\boldsymbol{g}}_0$ denotes $\tilde{\boldsymbol{g}}$ in the reference configuration in the nematic phase. The normalized step-length tensor $\tilde{\boldsymbol{g}}$ can be expressed as

$$\tilde{\boldsymbol{g}} = \tilde{g}_{\perp}\left[\mathbf{I} + \left(\frac{\tilde{g}_{\parallel}}{\tilde{g}_{\perp}} - 1\right)\boldsymbol{n}\otimes\boldsymbol{n}\right], \boldsymbol{n} = \frac{\mathbf{F}\boldsymbol{n}_0}{|\mathbf{F}\boldsymbol{n}_0|}, \tag{A2}$$

where $\tilde{g}_{\parallel}$ and $\tilde{g}_{\perp}$ are eigenvalues of $\tilde{\boldsymbol{g}}$ parallel and perpendicular to the director, respectively, satisfying $\tilde{g}_{\parallel}\tilde{g}_{\perp}^2 = 1$, $\boldsymbol{I}$ is a 3-by-3 identity matrix, $\boldsymbol{n}$ is a unit vector along the director, and $\boldsymbol{n}_0$ denotes $\boldsymbol{n}$ in the reference configuration. The prescribed metric tensor $\bar{\boldsymbol{a}}$ that maps the reference configuration in the nematic phase to the current configuration can be expressed as $\bar{\boldsymbol{a}} = \tilde{\boldsymbol{g}}\tilde{\boldsymbol{g}}_0^{-1}$, yielding the prescribed stretch λ along the director as the following, according to Eq. (1)

$$\lambda = \sqrt{\tilde{g}_{\parallel}/\tilde{g}_{0\parallel}}, \tag{A3}$$

where $\tilde{g}_{0\parallel}$ is the eigenvalue of $\tilde{\boldsymbol{g}}_0$ parallel to the director. We fit the stretch-temperature relation to the experimental data and obtain

$$\lambda = 0.6\sqrt{1 + 1.778^{\frac{120-T}{60}}}, 60℃ \leq T \leq 120℃. \tag{A4}$$

The above stretch-temperature relation indicates that nematic LCEs start to deform at 60 ℃ and continuously deform until 120 ℃, yielding a maximum stretch of 0.6 parallel to the director. Using Eq. (A4), prescribed stretch patterns were converted into temperature distributions, which are assigned to LCE sheets as predefined fields in FE simulations.

We used the commercial software Abaqus/Standard for our FE simulations. We implemented the free energy in Eq. (A1) in Abaqus by writing a user-defined material subroutine (UMAT) (Supplementary material). The element type is the 3D hybrid quadratic brick with reduced integration (Abaqus type C3D20RH). A mesh refinement study was performed to ensure that there are at least three elements along the thickness and that the aspect ratio of a single element is no greater than 5. As a result, approximately 3 × 10^4 elements are involved in each finite element model. The LCE sheets in all the simulations have free boundary conditions. Artificial damping was introduced into the static general procedure such that a LCE sheet can snap to a stable equilibrium state when loss of stability occurs. The damping factor in the simulations was determined based on the fraction of dissipated energy; it is set as 1×10^{-5}, a value that can suppress instabilities without having a significant effect on the solutions.

5. Energy minimization using variational approach

The minimization of elastic energy E_{total} in Eq. (6) can be performed by a variational approach. The total elastic energy E_{total} can be expressed as a functional in terms of functions $E(v)$, $G(v)$, integration constant c, and variable v,

$$E_{\mathrm{total}} = \mu L \int_0^w Q[E(v), E'(v), E''(v), G(v), G'(v), c, v]\,\mathrm{d}v. \tag{A5}$$

Taking variation of E_{total} with respect to $E(v)$, $G(v)$, and c, and setting the first variation to be zero give the following Euler-Lagrange equations

$$\frac{\partial Q}{\partial E} - \left(\frac{\partial Q}{\partial E'}\right)' + \left(\frac{\partial Q}{\partial E''}\right)'' = 0, \tag{A6}$$

$$\frac{\partial Q}{\partial G} - \left(\frac{\partial Q}{\partial G'}\right)' = 0, \tag{A7}$$

$$\frac{\partial Q}{\partial c} = 0, \tag{A8}$$

and boundary conditions at $v = 0$ and w

$$\frac{\partial Q}{\partial E'} - \left(\frac{\partial Q}{\partial E''}\right)' = 0, \tag{A9}$$

$$\frac{\partial Q}{\partial E''} = 0, \tag{A10}$$

$$\frac{\partial Q}{\partial G'} = 0. \tag{A11}$$

From Eq. (A8), we can express c in terms of $E(v)$,$E'(v)$,$E''(v)$,$G(v)$, and $G'(v)$. Substituting this expression of c into Eqs. (A6-7) and (A9-11) yields a sixth-order ODE system, which can be solved by the ODE solver (bvp4c) in Matlab.

6. 3D surfaces reconstruction given metric and curvature tensors

A 3D surface with metric tensor ***a*** and curvature tensor ***b*** satisfying Gauss and Mainardi-Codazzi equations[36,38] can be reconstructed using the following method. Let

$$\boldsymbol{r}(u,v) = (x(u,v),y(u,v), z(u,v)\,) \tag{A12}$$

be a parametrization of a 3D surface S with the following ***a*** and ***b***

$$\boldsymbol{a} = \begin{bmatrix} E(u,v) & F(u,v) \\ F(u,v) & G(u,v) \end{bmatrix}, \boldsymbol{b} = \begin{bmatrix} e(u,v) & f(u,v) \\ f(u,v) & g(u,v) \end{bmatrix}, \tag{A13}$$

where u $(u_{\min} \leq u \leq u_{\max})$ and v $(v_{\min} \leq v \leq v_{\max})$ are the two surface coordinates, as shown in Fig. 2A $(u_{\min} = 0, u_{\max} = L, v_{\min} = 0,$ and $v_{\max} = w)$. Every point on the surface S has a local frame formed by the vectors $\boldsymbol{r}_{,u}$, $\boldsymbol{r}_{,v}$ and $\boldsymbol{N}$, where $(\ )_{,u}$ and $(\ )_{,v}$ denote partial derivative of ( ) with respect to u and v, respectively, and $\boldsymbol{N}$ is the normal vector of the surface S. The derivatives of the vectors $\boldsymbol{r}_{,u}$, $\boldsymbol{r}_{,v}$ and $\boldsymbol{N}$ can be expressed in the basis $\{\boldsymbol{r}_{,u}, \boldsymbol{r}_{,v}, \boldsymbol{N}\,\}$ as[38]

$$\begin{gathered} \boldsymbol{r}_{,uu} = \Gamma_{11}^{1}\boldsymbol{r}_{,u} + \Gamma_{11}^{2}\boldsymbol{r}_{,v} + e\boldsymbol{N}, \\ \boldsymbol{r}_{,uv} = \Gamma_{12}^{1}\boldsymbol{r}_{,u} + \Gamma_{12}^{2}\boldsymbol{r}_{,v} + f\boldsymbol{N}, \\ \boldsymbol{r}_{,vv} = \Gamma_{22}^{1}\boldsymbol{r}_{,u} + \Gamma_{22}^{2}\boldsymbol{r}_{,v} + g\boldsymbol{N}, \\ \boldsymbol{N}_{,u} = \alpha_1\boldsymbol{r}_{,u} + \alpha_2\boldsymbol{r}_{,v}, \\ \boldsymbol{N}_{,v} = \beta_1\boldsymbol{r}_{,u} + \beta_2\boldsymbol{r}_{,v}, \end{gathered} \tag{A14}$$

where the coefficient Γ_{ij}^{k} $(i, j, k = 1, 2)$ are the Christoffel symbols of S, which can be computed in terms of E, F, G and their derivatives,

$$\begin{gathered}\Gamma^1_{11} = \frac{GE_{,u} + FE_{,v} - 2FF_{,u}}{2(EG - F^2)}, \Gamma^2_{11} = \frac{2EF_{,u} - FE_{,u} - EE_{,v}}{2(EG - F^2)}, \\ \Gamma^1_{12} = \Gamma^1_{21} = \frac{GE_{,v} - FG_{,u}}{2(EG - F^2)}, \Gamma^2_{12} = \Gamma^2_{21} = \frac{EG_{,u} - FE_{,v}}{2(EG - F^2)}, \\ \Gamma^1_{22} = \frac{-FG_{,v} - GG_{,u} + 2GF_{,v}}{2(EG - F^2)}, \Gamma^2_{22} = \frac{EG_{,v} + FG_{,u} - 2FF_{,v}}{2(EG - F^2)},\end{gathered} \tag{A15}$$

and

$$\alpha_1 = \frac{fF - eG}{EG - F^2}, \alpha_2 = \frac{eF - fE}{EG - F^2}, \beta_1 = \frac{gF - fG}{EG - F^2}, \beta_2 = \frac{fF - gE}{EG - F^2}. \tag{A16}$$

We first fix $u = u_{\min}$, and set $y_1 = \boldsymbol{r}$, $y_2 = \boldsymbol{r}_{,v}$, $y_3 = \boldsymbol{N}$, $y_4 = \boldsymbol{r}_{,u}$. Eq. (A14) can be rewritten as

$$\frac{d}{dv}\begin{bmatrix} y_1 \\ y_2 \\ y_3 \\ y_4 \end{bmatrix} = \begin{bmatrix} 0 & 1 & 0 & 0 \\ 0 & \Gamma^2_{22} & g & \Gamma^1_{22} \\ 0 & \beta_2 & 0 & \beta_1 \\ 0 & \Gamma^2_{12} & f & \Gamma^1_{12} \end{bmatrix}\begin{bmatrix} y_1 \\ y_2 \\ y_3 \\ y_4 \end{bmatrix}, \tag{A17}$$

which can be solved numerically under the following initial values

$$\begin{gathered} y_1|_{u\,=\,u_{\min},\, v\,=\,v_{\min}} = \boldsymbol{r}|_{u\,=\,u_{\min},\, v\,=\,v_{\min}} = (0, 0, 0) \\ y_2|_{u\,=\,u_{\min},\, v\,=\,v_{\min}} = \boldsymbol{r}_{,v}|_{u\,=\,u_{\min},\, v\,=\,v_{\min}} = \left(\frac{F_0}{\sqrt{E_0}}, \sqrt{\frac{E_0G_0 - F_0^2}{E_0}}, 0\right) \\ y_3|_{u\,=\,u_{\min},\, v\,=\,v_{\min}} = \boldsymbol{N}|_{u\,=\,u_{\min},\, v\,=\,v_{\min}} = (0, 0, 1) \\ y_4|_{u\,=\,u_{\min},\, v\,=\,v_{\min}} = \boldsymbol{r}_{,u}|_{u\,=\,u_{\min},\, v\,=\,v_{\min}} = \left(\sqrt{E_0}, 0, 0\right) \end{gathered}, \tag{A18}$$

where E_0, F_0, and G_0 are the components of the metric tensor $\boldsymbol{a}$ at the point ($u_{\min}$, $v_{\min}$). Then we uniformly discretize the domain of v with small increments. For a given v_i ($v_{\min} \le v_i \le v_{\max}$), we can set $x_1 = \boldsymbol{r}$, $x_2 = \boldsymbol{r}_{,u}$, $x_3 = \boldsymbol{N}$, $x_4 = \boldsymbol{r}_{,v}$, and rewrite Eq. (A7) as

$$\frac{d}{du}\begin{bmatrix} x_1 \\ x_2 \\ x_3 \\ x_4 \end{bmatrix} = \begin{bmatrix} 0 & 1 & 0 & 0 \\ 0 & \Gamma^1_{11} & e & \Gamma^2_{11} \\ 0 & \alpha_1 & 0 & \alpha_2 \\ 0 & \Gamma^1_{12} & f & \Gamma^2_{12} \end{bmatrix}\begin{bmatrix} x_1 \\ x_2 \\ x_3 \\ x_4 \end{bmatrix}, \tag{A19}$$

which can be solved numerically under the following initial values

$$\begin{gathered} x_1\big|_{u=u_{\min},\, v=v_i} = \boldsymbol{r}\big|_{u=u_{\min},\, v=v_i} = y_1\big|_{u=u_{\min},\, v=v_i} \\ x_2\big|_{u=u_{\min},\, v=v_i} = \boldsymbol{r}_{,u}\big|_{u=u_{\min},\, v=v_i} = y_4\big|_{u=u_{\min},\, v=v_i} \\ x_3\big|_{u=u_{\min},\, v=v_i} = \boldsymbol{N}\big|_{u=u_{\min},\, v=v_i} = y_3\big|_{u=u_{\min},\, v=v_i} \\ x_4\big|_{u=u_{\min},\, v=v_i} = \boldsymbol{r}_{,v}\big|_{u=u_{\min},\, v=v_i} = y_2\big|_{u=u_{\min},\, v=v_i} \end{gathered}. \tag{A20}$$

Thus far, we have obtained the parameterization ***r*** of surface *S* based on the metric tensor ***a*** and curvature tensor ***b***.

7. Decomposition of a prescribed metric tensor $\bar{\boldsymbol{a}}$

The position vector of a point on a 2D surface with the metric tensor $\bar{\boldsymbol{a}}$ (Eq. (1)) in Euclidean 3D space can be expressed as

$$\bar{\boldsymbol{\rho}}(u,v) = x(u)\boldsymbol{e}_u + y(v)\boldsymbol{e}_v, \tag{A21}$$

where u and v are surface coordinates, $\boldsymbol{e}_u$ and $\boldsymbol{e}_v$ are the base vectors in Cartesian coordinate system, and $x(u)$ and $y(v)$ are the corresponding position components, respectively. Given $\bar{\boldsymbol{a}}$ in Eq. (1), we obtain

$$\frac{\partial x}{\partial u} = \lambda_u \text{ and } \frac{\partial y}{\partial v} = \lambda_v. \tag{A22}$$

This 2D surface with $\bar{\boldsymbol{a}}$ can be formed by the following three deformation steps. The first step is applying a stretch λ_v in the v direction, yielding the following position vector $\bar{\boldsymbol{\rho}}_1$ and corresponding metric tensor $\bar{\boldsymbol{a}}_1$,

$$\bar{\boldsymbol{\rho}}_1(u,v) = u\boldsymbol{e}_u + \int_0^v \lambda_v(\tau)\mathrm{d}\tau \boldsymbol{e}_v,\ \bar{\boldsymbol{a}}_1 = \begin{bmatrix} 1 & 0 \\ 0 & \lambda_v^2 \end{bmatrix}. \tag{A23}$$

Set $v^* = \int_0^v \lambda_v(\tau)\mathrm{d}\tau$ and apply the coordinate transformation from (u,v) to (u,v^*), we have

$$\bar{\boldsymbol{\rho}}_1(u,v^*) = u\boldsymbol{e}_u + v^*\boldsymbol{e}_v. \tag{A24}$$

The next step is applying a homogeneous stretch $\bar{\lambda}_u$ in the u direction, yielding the following position vector $\bar{\boldsymbol{\rho}}_2$ and corresponding metric tensor $\bar{\boldsymbol{a}}_2$,

$$\bar{\boldsymbol{\rho}}_2(u,v^*) = \bar{\lambda}_u u \boldsymbol{e}_u + v^* \boldsymbol{e}_v,\ \bar{\boldsymbol{a}}_2 = \begin{bmatrix} (\bar{\lambda}_u)^2 & 0 \\ 0 & 1 \end{bmatrix}. \tag{A25}$$

We change the coordinates from (u,v^*) to (u^*,v^*) by setting $u^* = \bar{\lambda}_u u$. Then, $\bar{\boldsymbol{\rho}}_2$ can be rewritten as

$$\bar{\boldsymbol{\rho}}_2(u^*,v^*) = u^* \boldsymbol{e}_u + v^* \boldsymbol{e}_v. \tag{A26}$$

The third step is applying stretches λ_u^* in the u^* direction, yielding the following position vector $\bar{\boldsymbol{\rho}}^*$ and corresponding metric tensor $\bar{\boldsymbol{a}}^*$,

$$\bar{\boldsymbol{\rho}}^*(u^*,v^*) = x^*(u^*) \boldsymbol{e}_u + v^* \boldsymbol{e}_v,\ \bar{\boldsymbol{a}}^* = \begin{bmatrix} (\lambda_u^*)^2 & 0 \\ 0 & 1 \end{bmatrix}, \tag{A27}$$

where $\lambda_u^* = \frac{\partial x^*}{\partial u^*}$. To ensure that applying $\bar{\boldsymbol{a}}_1$, $\bar{\boldsymbol{a}}_2$, and $\bar{\boldsymbol{a}}^*$ sequentially yields a surface with metric tensor $\bar{\boldsymbol{a}}$, $\bar{\boldsymbol{\rho}}$ should equal $\bar{\boldsymbol{\rho}}^*$. Therefore, $x(u) = x^*(u^*)$ and $y(v) = v^*$. With Eq. (A22), we have

$$\lambda_u = \lambda_u^* \bar{\lambda}_u. \tag{A28}$$

Acknowledgement

Y.C. and L.J. acknowledge the support from the National Science Foundation through Grant No. CMMI-1925790. A.S.K. and R.C.H. acknowledge support from the Office of Naval Research through the MURI on Photomechanical Materials (ONR N00014-18-1-2624). This work used computational and storage services associated with the Hoffman2 Shared Cluster provided by Institute for Digital Research and Education's Research Technology Group at the University of California, Los Angeles.

Reference

1 Y. Klein, E. Efrati and E. Sharon, *Science*, 2007, **315**, 1116–1120.

2 J. Kim, J. A. Hanna, M. Byun, C. D. Santangelo and R. C. Hayward, *Science*, 2012, **335**, 1201–1205.

3 A. Sydney Gladman, E. A. Matsumoto, R. G. Nuzzo, L. Mahadevan and J. A. Lewis, *Nat. Mater.*, 2016, **15**, 413–418.

4 S.-J. Jeon, A. W. Hauser and R. C. Hayward, *Acc. Chem. Res.*, 2017, **50**, 161–169.

5 T. J. White and D. J. Broer, *Nat. Mater.*, 2015, **14**, 1087–1098.

6 R. S. Kularatne, H. Kim, J. M. Boothby and T. H. Ware, *J. Polym. Sci. Part B Polym. Phys.*, 2017, **55**, 395–411.

7 T. H. Ware, M. E. McConney, J. J. Wie, V. P. Tondiglia and T. J. White, *Science*, 2015, **347**, 982–984.

8 Y. Xia, G. Cedillo-Servin, R. D. Kamien and S. Yang, *Adv. Mater.*, 2016, **28**, 9637–9643.

9 B. A. Kowalski, V. P. Tondiglia, T. Guin and T. J. White, *Soft Matter*, 2017, **13**, 4335–4340.

10 A. S. Kuenstler, Y. Chen, P. Bui, H. Kim, A. DeSimone, L. Jin and R. C. Hayward, *Adv. Mater.*, 2020, **32**, 2000609.

11 Q. Zhao, H. J. Qi and T. Xie, *Prog. Polym. Sci.*, 2015, **49–50**, 79–120.

12 A. Lendlein and O. E. C. Gould, *Nat. Rev. Mater.*, 2019, **4**, 116–133.

13 C. L. Randall, E. Gultepe and D. H. Gracias, *Trends Biotechnol.*, 2012, **30**, 138–146.

14 S. J. Woltman, G. D. Jay and G. P. Crawford, *Nat. Mater.*, 2007, **6**, 929–938.

15 L. Ionov, *Langmuir*, 2015, **31**, 5015–5024.

16 C. Ohm, M. Brehmer and R. Zentel, *Adv. Mater.*, 2010, **22**, 3366–3387.

17 J. L. Silverberg, J.-H. Na, A. A. Evans, B. Liu, T. C. Hull, C. D. Santangelo, R. J. Lang, R. C. Hayward and I. Cohen, *Nat. Mater.*, 2015, **14**, 389–393.

18 Y. Tang, Y. Li, Y. Hong, S. Yang and J. Yin, *Proc. Natl. Acad. Sci.*, 2019, **116**, 26407–26413.

19 T. van Manen, S. Janbaz and A. A. Zadpoor, *Mater. Today*, 2018, **21**, 144–163.

20 E. Sharon and E. Efrati, *Soft Matter*, 2010, **6**, 5693.

21 J. Kim, J. A. Hanna, R. C. Hayward and C. D. Santangelo, *Soft Matter*, 2012, **8**, 2375.

22 M. Byun, C. D. Santangelo and R. C. Hayward, *Soft Matter*, 2013, **9**, 8264.

23 L. T. de Haan, C. Sánchez-Somolinos, C. M. W. Bastiaansen, A. P. H. J. Schenning and D. J. Broer, *Angew. Chem. Int. Ed.*, 2012, **51**, 12469–12472.

24 A. Kotikian, R. L. Truby, J. W. Boley, T. J. White and J. A. Lewis, *Adv. Mater.*, 2018, **30**, 1706164.

25 C. P. Ambulo, J. J. Burroughs, J. M. Boothby, H. Kim, M. R. Shankar and T. H. Ware, *ACS Appl. Mater. Interfaces*, 2017, **9**, 37332–37339.

26 Y. Cheng, H. Lu, X. Lee, H. Zeng and A. Priimagi, *Adv. Mater.*, 2020, **32**, 1906233.

27 C. D. Modes, K. Bhattacharya and M. Warner, *Proc. R. Soc. Math. Phys. Eng. Sci.*, 2011, **467**, 1121–1140.

28 T. Guin, M. J. Settle, B. A. Kowalski, A. D. Auguste, R. V. Beblo, G. W. Reich and T. J. White, *Nat. Commun.*, 2018, **9**, 2531.

29 H. Aharoni, E. Sharon and R. Kupferman, *Phys. Rev. Lett.*, 2014, **113**, 257801.

30 P. Plucinsky, B. A. Kowalski, T. J. White and K. Bhattacharya, *Soft Matter*, 2018, **14**, 3127–3134.

31 B. A. Kowalski, C. Mostajeran, N. P. Godman, M. Warner and T. J. White, *Phys. Rev. E*, 2018, **97**, 012504.

32 H. Aharoni, Y. Xia, X. Zhang, R. D. Kamien and S. Yang, *Proc. Natl. Acad. Sci.*, 2018, **115**, 7206–7211.

33 E. Efrati, E. Sharon and R. Kupferman, *J. Mech. Phys. Solids*, 2009, **57**, 762–775.

34 E. Efrati, E. Sharon and R. Kupferman, *Phys. Rev. E*, 2009, **80**, 016602.

35 B. Audoly and Y. Pomeau, *Elasticity and geometry: from hair curls to the non-linear response of shells*, Oxford university press, 2010.

36 M. Moshe, E. Sharon and R. Kupferman, *Nonlinearity*, 2013, **26**, 3247–3258.

37 O. Oshri, S. Biswas and A. C. Balazs, *Phys. Rev. E*, 2019, **99**, 033003.

38 M. P. Do Carmo, *Differential geometry of curves and surfaces: revised and updated second edition*, Courier Dover Publications, 2016.

39 P. Bladon, E. Terentjev and M. Warner, *Phys. Rev. E*, 1993, **47**, R3838.

40 L. Jin, Z. Zeng and Y. Huo, *J. Mech. Phys. Solids*, 2010, **58**, 1907–1927.

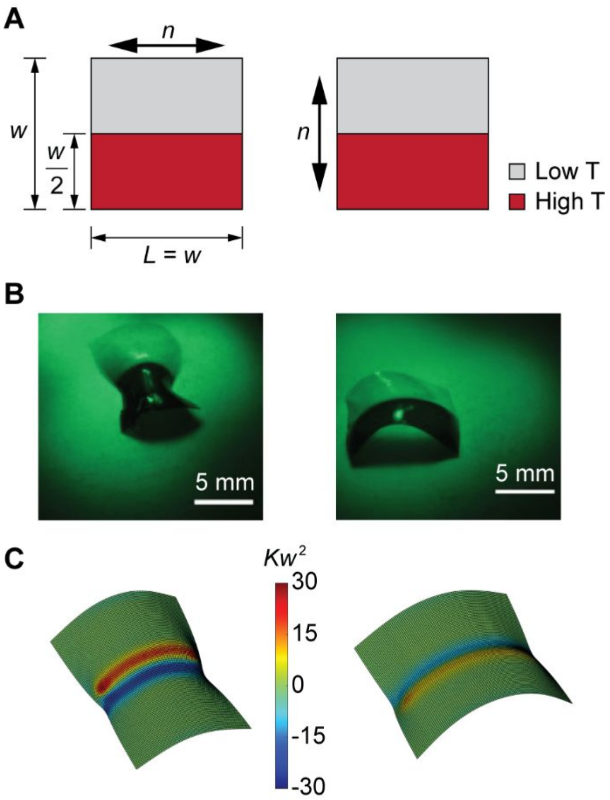

Fig. 1. Formation of rolled shapes from LCE bistrips induced by discretely patterned in-plane stretch profiles. (A) A monodomain LCE thin sheet is equally divided into high- and low-temperature strips. The initial director is either parallel (left) or perpendicular (right) to the interface between the two strips. (B) Experimentally, LCE bistrips are fabricated by spatially patterning the concentration of plasmonic gold nanoparticles; upon illumination, the transparent strip without nanoparticles is at low temperature and the dark strip with nanoparticles is at high temperature. These bistrips roll into nearly axisymmetric shapes with the symmetry axes perpendicular to the interface between the high- and low-temperature strips. (C) The rolled shapes can be captured by the FE simulations. The contours in (C) denote the distributions of normalized Gaussian curvatures.

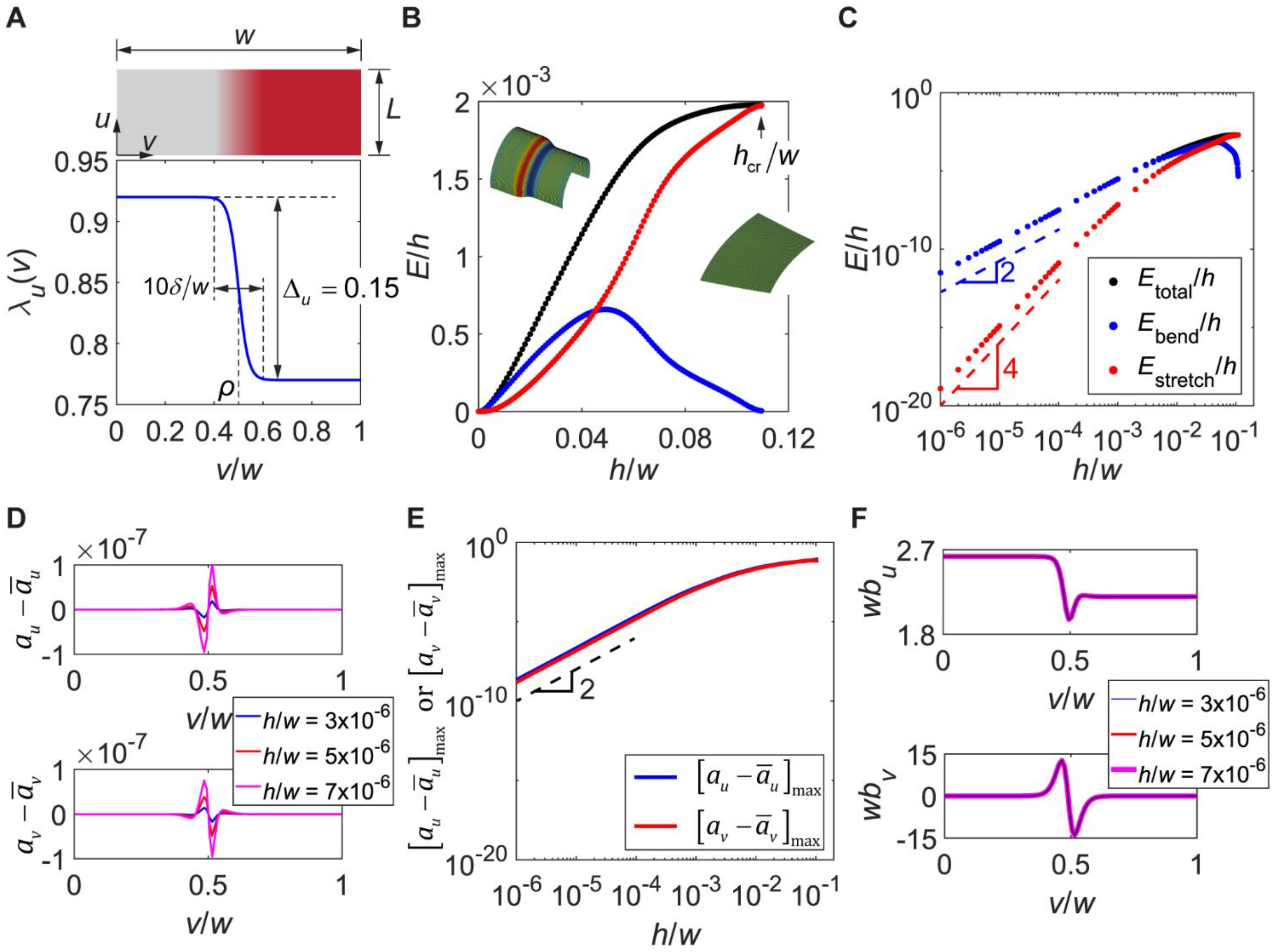

Fig. 2. Determination of rolled shapes. (A) Discretely patterned in-plane stretch profile with a step distribution in a LCE sheet. (B and C) Dependence of the energy on the thickness in linear (B) and logarithmic (C) scales for the case with $\rho = 0.5$, $L = 2w$, and initial director $\mathbf{n}$ parallel to the u direction. The dots in black, blue, and red colors represent the total, bending, and stretching elastic energies, respectively. (D) The distribution of the differences between the components of the actual metric tensor $\boldsymbol{a}$ and the prescribed metric tensor $\bar{\boldsymbol{a}}$ in the u (upper, $a_u - \bar{a}_u$) and v (lower, $a_v - \bar{a}_v$) directions when $h/w = 3 \times 10^{-6}$ (blue), 5×10^{-6} (red), and 7×10^{-6} (magenta). (E) Dependence of the maximum of $a_u - \bar{a}_u$ (blue) and $a_v - \bar{a}_v$ (red) on h/w. (F) Distribution of the normalized components of the curvature tensor $\boldsymbol{b}$ in the u (upper) and v (lower) directions when $h/w = 3 \times 10^{-6}$ (blue), 5×10^{-6} (red), and 7×10^{-6} (magenta).

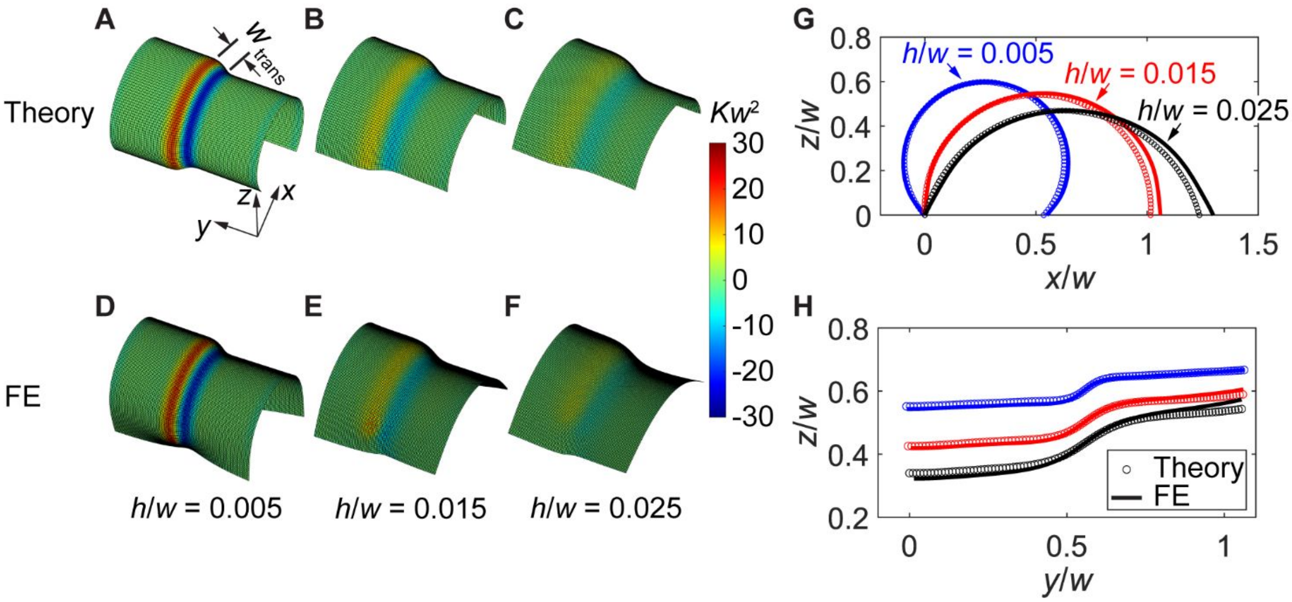

Fig. 3. Quantitative comparison between the theory and FE simulations. (A-F) The rolled shapes obtained from the theory (A-C) and FE simulations (D-F) for LCE bistrips with the director parallel to the interface between the high- and low-temperature regions and of normalized thickness h/w = 0.005 (A and D), 0.015 (B and E), and 0.025 (C and F). (G and H) The profiles of the cross-section along (G) and perpendicular to (H) the interface between the two strips. The circular dots represent analytical results, whereas the solid lines represent the results from FE simulations. The blue, red, and black colors denote h/w= 0.005, 0.015, and 0.025, respectively.

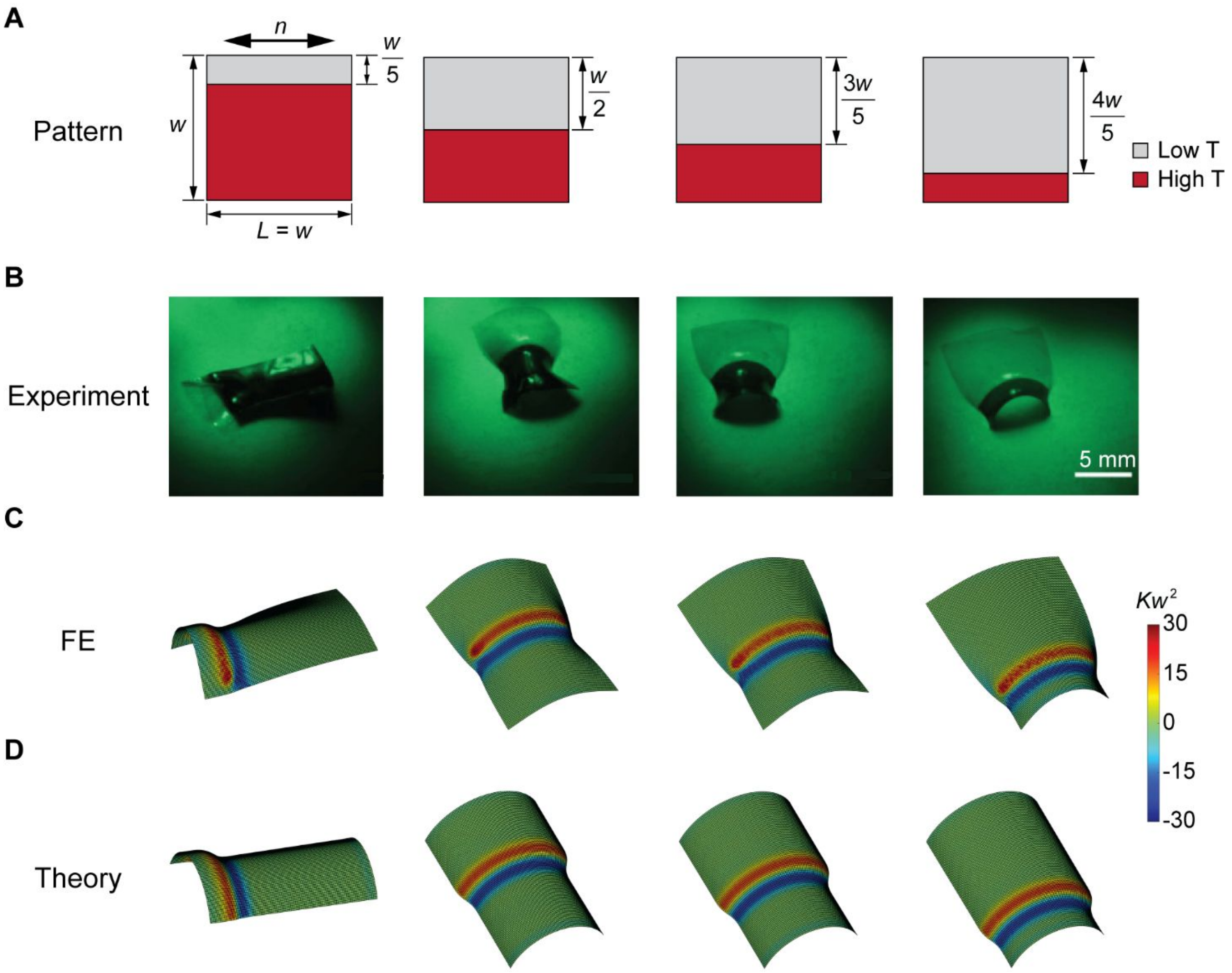

Fig. 4. Comparison of the rolled shapes obtained from experiments, FE simulations, and theory for LCE bistrips with different ρ. (A) Patterns of the prescribed temperature distribution, corresponding to the in-plane stretch distribution, with ρ = 0.2 (1st column), 0.5 (2nd column), 0.6 (3rd column), and 0.8 (4th column). (B-D) The corresponding 3D shapes obtained from experiments (B), FE simulations (C), and theory (D). All the square LCE bistrips have a thickness of $h/w = 0.005$ and initial director $\mathbf{n}$ parallel to the interface between the high- and low-temperature strips.

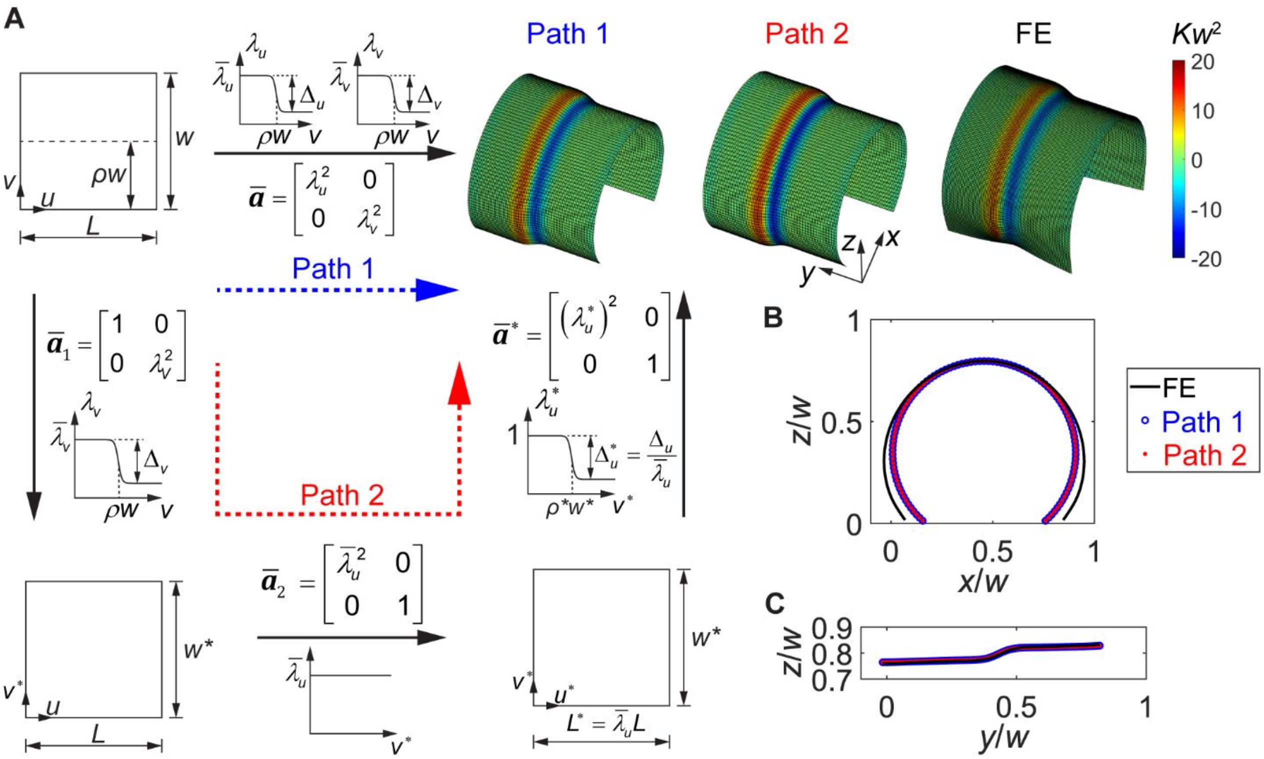

Fig. 5. Conversion from a prescribed metric tensor $\bar{\boldsymbol{a}}$ in LCE bistrips with initial director either parallel or perpendicular to the interface into a unified metric tensor $\bar{\boldsymbol{a}}^*$ embedded to a bistrip with modified geometry. (A) Shape morphing of a bistrip subjected to $\bar{\boldsymbol{a}}$ (Path 1) is equivalent to that of the bistrip with modified geometry subjected to $\bar{\boldsymbol{a}}^*$ (Path 2). The rolled shapes predicted by the analytical model following Path 1 and 2 and the FE simulation agree well. The profiles of the cross-section along (B) and perpendicular to (C) the interface between the high- and low-temperature strips based on Path 1 and 2 match perfectly.

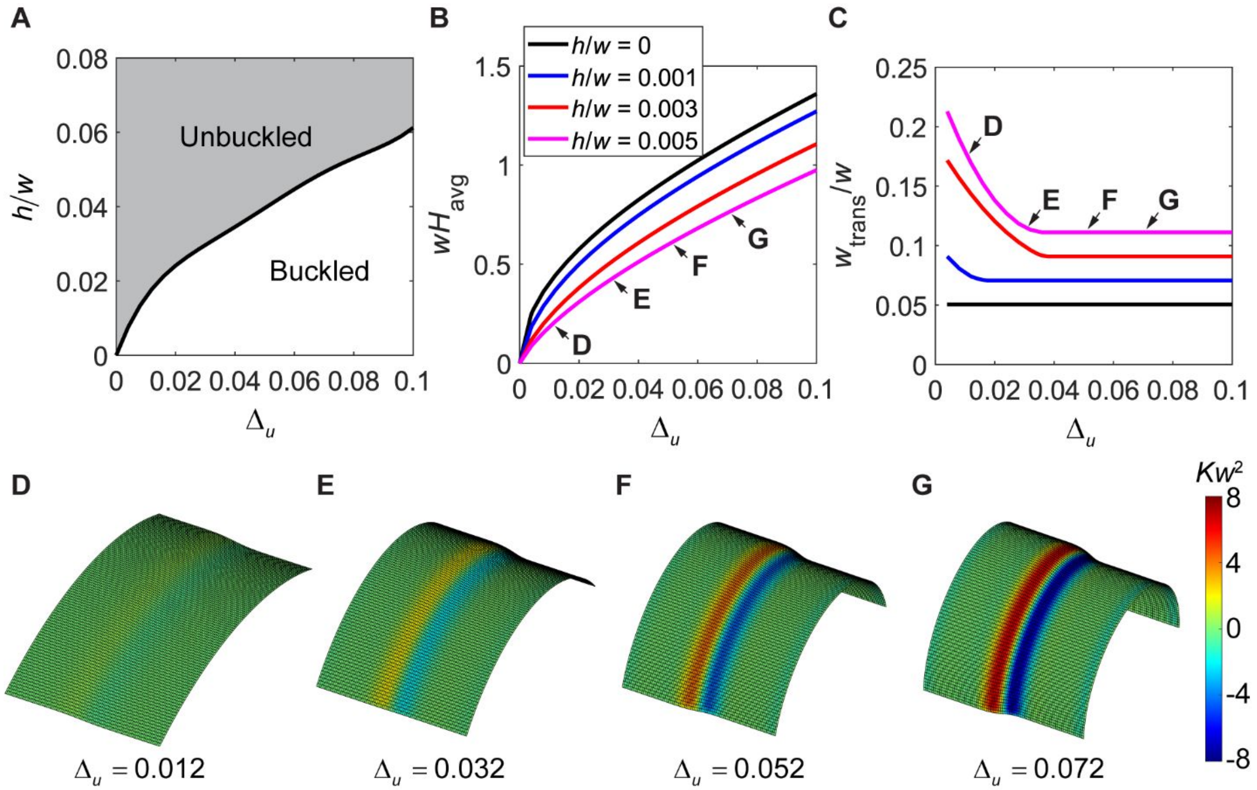

Fig. 6. The Effect of the stretch mismatch Δ_u on the rolled shapes when $\rho = 0.5$ and $\delta/w = 0.02$. (A) The dependence of the normalized critical thickness h_{cr}/w on Δ_u (black solid line). The gray region ($h/w > h_{\mathrm{cr}}/w$) indicates unbuckled configurations, whereas the white region ($h/w < h_{\mathrm{cr}}/w$) indicates buckled configurations. (B and C) The influence of Δ_u on the normalized average mean curvature wH_{avg} (B) and the width of the transitional bottle neck region w_{trans}/w (C) when $h/w = 0$ (isometric immersion in black), 0.001 (blue), 0.003 (red), and 0.005 (magenta). (D-G) The rolled shapes obtained from the theory for different Δ_u when $h/w = 0.005$.

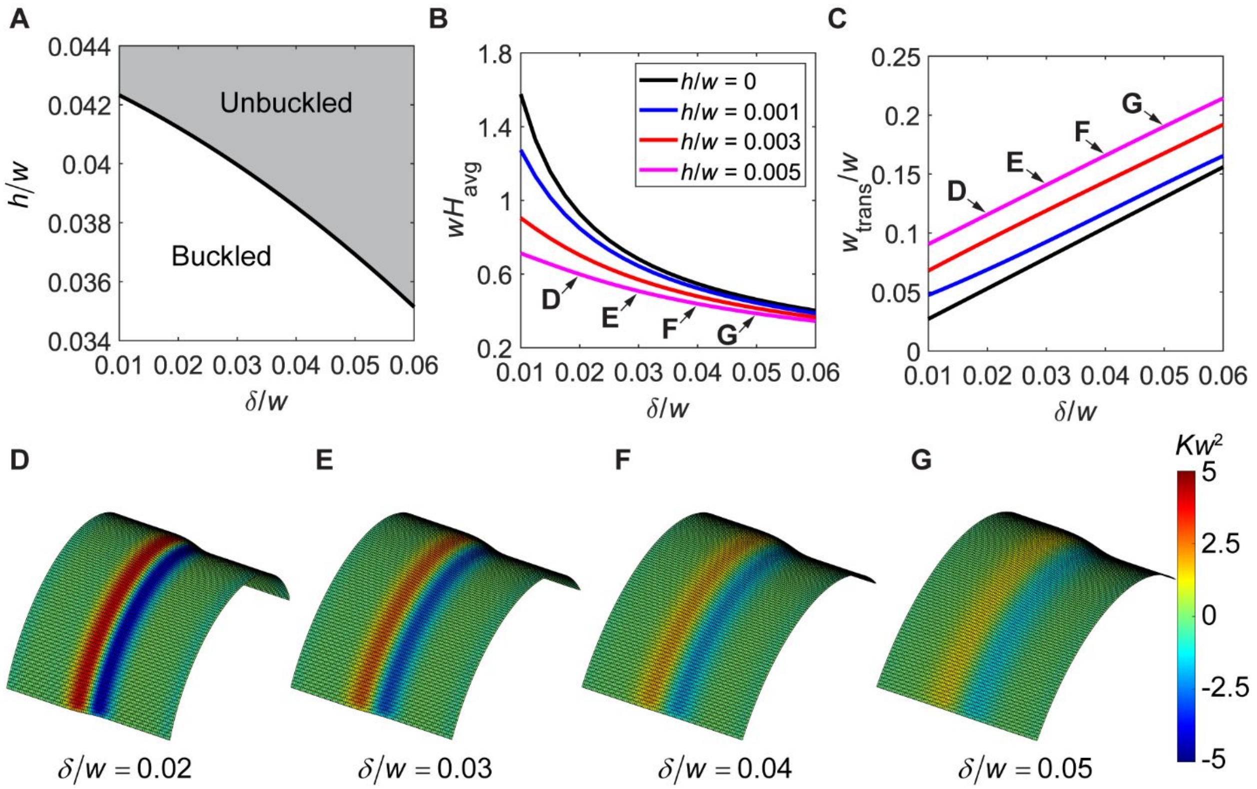

Fig. 7. The Effect of δ on the rolled shapes when $\rho = 0.5$ and $\Delta_u = 0.05$. (A) The dependence of h_{cr}/w on δ (black solid line). The gray region ($h/w > h_{\mathrm{cr}}/w$) indicates unbuckled configurations, whereas the white region ($h/w < h_{\mathrm{cr}}/w$) indicates buckled configurations. (B and C) The influence of δ on wH_{avg} (B) and w_{trans}/w (C) when $h/w = 0$ (isometric immersion in black), 0.001 (blue), 0.003 (red), and 0.005 (magenta). (D-G) The rolled shapes obtained from the theory for different δ when $h/w = 0.005$.

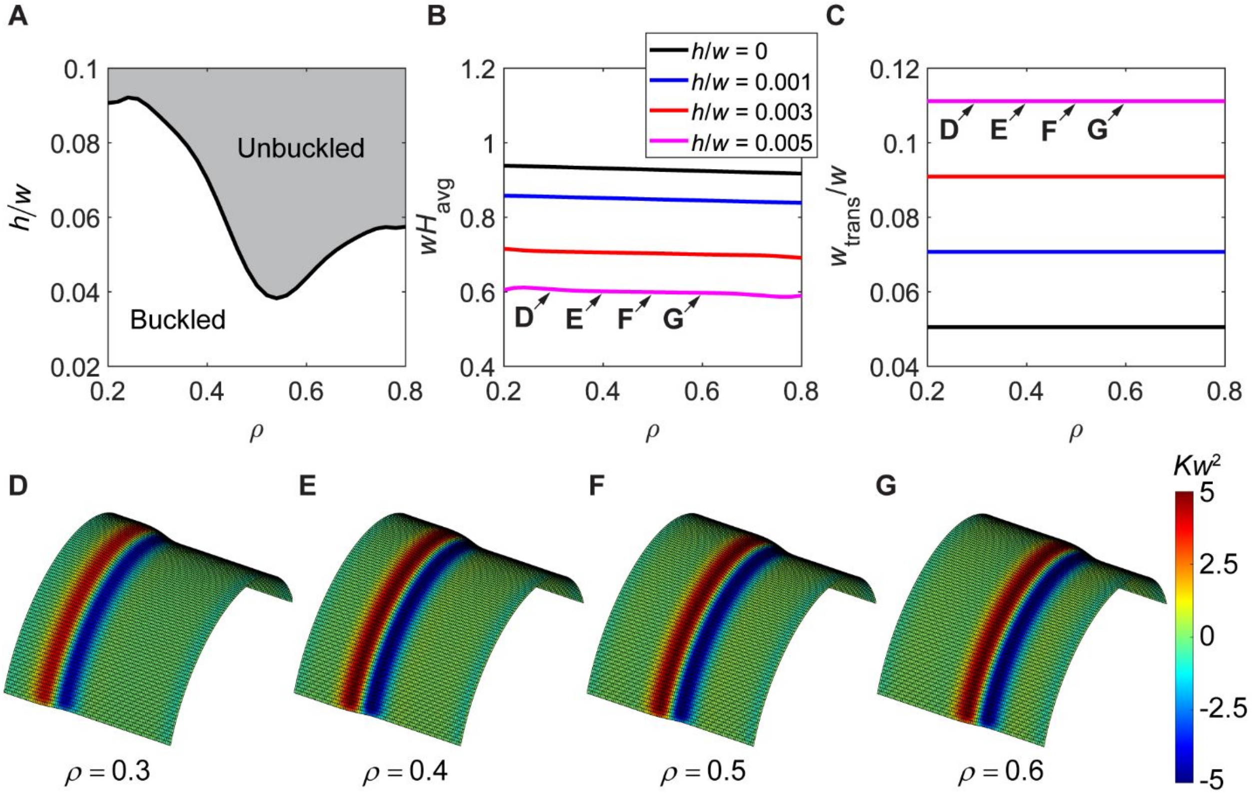

Fig. 8. The Effect of ρ on the rolled shapes when $\delta/w = 0.02$ and $\Delta_u = 0.05$. (A) The dependence of h_{cr}/w on ρ (black solid line). The gray region ($h/w > h_{\mathrm{cr}}/w$) indicates unbuckled configurations, whereas the white region ($h/w < h_{\mathrm{cr}}/w$) indicates buckled configurations. (B and C) The influence of ρ on wH_{avg} (B) and w_{trans}/w (C) when $h/w =$ 0 (isometric immersion in black), 0.001 (blue), 0.003 (red), and 0.005 (magenta). (D-G) The rolled shapes obtained from the theory for different ρ when $h/w =$ 0.005.